Check for
updates

An airlight estimation method for image dehazing based on gray projection

Wencheng Wang [1] · Xiaohui Yuan [2] · Xiaojin Wu [1] · Yihua Dong [1]

Abstract

As the key parameter of dehazing algorithms, airlight value directly affect the calculation accuracy of sky region, and any deviation will lead to the chromatic aberration in the image restoration. Many methods are proposed to address this problem, but the large amount of calculation or large deviations make them difficult to apply to real-time systems. In this paper, a fast algorithm is proposed based on the statistics of sky area's distribution in hazy images. Firstly, fast mean filter is used to process gray image; and then the anti-interference ability of regional projection is analysied. Through the horizontal projection and vertical projection, the main sky area is quickly located, and finally the sky region are calculated by selecting some special pixels as atmospheric light. A large number of experiments show that the proposed algorithm can obtain the airlight value quickly for the images with sky region, and can be used in real-time conditions.

1 Introduction

Hazy weather is a natural phenomenon caused by the scattering of atmospheric particles in the air. This type of weather often causes a significant decrease in the contrast and visibility of collected images, which affects the performance of outdoor visual systems. The use of information processing techniques for image dehazing can effectively resolve image quality degradation, raise the visibility of observation scenes, and improve the robustness of outdoor systems in target recognition and tracking. At present, the processing methods for hazy images

✉ Wencheng Wang
   wwcwfu@126.com

1   College of Information and Control Engineering, Weifang University, Weifang, China

2   Department of Computer Science and Engineering, University of North Texas, Denton, TX, USA

are usually divided into two classes: enhancement-based methods and restoration-based methods. Image enhancement-based methods improve the visual effect of images by improving the contrast of degraded images, which mainly include the histogram equalization method [18], Retinex method [5], homomorphic filtering method [33], wavelet transform method [6], etc.. Although these algorithms can visually improve the quality of an image, they do not consider image degradation factors, which often cause color distortion in recovered images. Image restoration-based methods usually compensate for missing information of hazy image via an inversion operation by establishing a degradation model for the physical process. This kind methods have high directivity with the natural effect of a dehazed image, attracted attention from many researchers in recent years, and has achieved productive results [1, 3, 15, 16, 21, 43].

For instance, Narasimhan et al. [26] estimated the depth information to restore a clear image based on a physical model by specifying the maximum depth of field and the minimum depth of field. Hautiere et al. [11] applied a vehicle sensor to calculate the depth of the scence and adopted a three-dimensional geographic model for dehazing. Kopf et al. [19] employed a terrain map and achieved the goal of dehazing by building a three-dimensional model with some known information. This type of method was established on the premise of known depth; the effect of the restored image is good, but the depth information of the known scene is required. Schechner et al. [32] photographed multiple images with different polarizing angles in the same scene by applying polarization characteristics of skylight and restored the degraded image via depth information estimation from the obtained polarization. Narasimhan and Nayar [28] used two images with the same scene and different weather conditions to obtain the depth information of an image and obtained satisfied results. These two restoration methods require multiple different images of the same scene; however, the source images are difficult to obtain in an actual application.

In the late years, the prior knowledge based single-image dehazing algorithm has become the focus of research. For instance, Tan [36] implemented image defogging by maximizing image contrast based on the hypothesis that a fogless image has higher contrast than a foggy image. Nevertheless, the method is easy to cause image oversaturation. Fattal [8], the author presume that the chrominance of an object and the media propagation have uncorrelated local statistics, which can be estimated by a scene albedometer via independent component analysis. This method is not suitable for image dehazing in heavy foggy weather. Fattal [9] proposed the use of color lines of an image-local block as a prior condition to optimize the atmospheric transmittance. Based on the statistical characteristics of the pixel distribution for a large number of fogless images, In Ref. [12], a dark channel prior (DCP) method is presented for dehazing method. This algorithm adopts a minimum filtering to caculate the media propagation function and optimizes estimation to obtain a better effect. Tarel and Hautiere [37] estimated the atmospheric distribution with a median filter; however, this approach can easily induce the halo effect at the edge region with abrupt changes in field depth. Dong et al. [7] adopted a modified physical model of a hazy image to dehaze it via the introduction of additive Gaussian white noise. However, the iterative solution exhibited a higher time complexity for the method. Kratz and Nishino [20], Nishino et al. [29] presumed that hazy images are composed of two independent parts the albedo layer and the depth layer. The MRF(Markov Random Field) idea and Bayes' probability methods were employed for analysis. However, some of the pixel colors in the resulting image were

oversaturated. Ancuti and Ancuti [2] adopt the idea of image fusion for image dehazing firstly, and then, Wang and Feng [41] presented a dehazing algorithm by transmission fusion subsequently. Gibson and Nguyen [10] used a Wiener filter for fast single-image dehazing, and Meng et al. [25] take the regularization method used for dehazing. Kim et al. [17] developed a cost function of image contrast and information loss, and proposed an effective method. Zhu et al. [51] presented a color attenuation prior method, which is simple and relatively novel. Wang et al. [44] suggested an image dehazing method for a large area of the sky region, which obtained good results for the restoration of an image containing sky.

Of these algorithms, the DCP-based method proposed by He et al. [12] has been investigated by a significant number of researchers due to its clear principle and significant performance. Yet, this algorithm adopted soft matting for transmission map refining and caused a slow calculation speed. Various of optimization algorithms were proposed to accelerate the speed of transmission refinement, e.g. guided filter [13], bilateral filter [46, 47], anisotropic filter [38], edge-preserving filter [34], median filter [14], and weighted guided filter [23], which improved the speed of calculation to a certain extent and continued to perfect the algorithm [39, 45]. Currently, numerous research results of transmission rate estimation in physical model-based image dehazing algorithms have been obtained; however, the airlight values are usually calculated with simple rules [32]. Inaccurate airlight value will cause the color distortion of restored image. As shown in Fig. 1, (a) is a hazy image; (b) is the restored image with color shift. It can be seen that the error of airlight can cause an image color shift, which will directly affect the authenticity of the image. (c) is the over-brighten image after
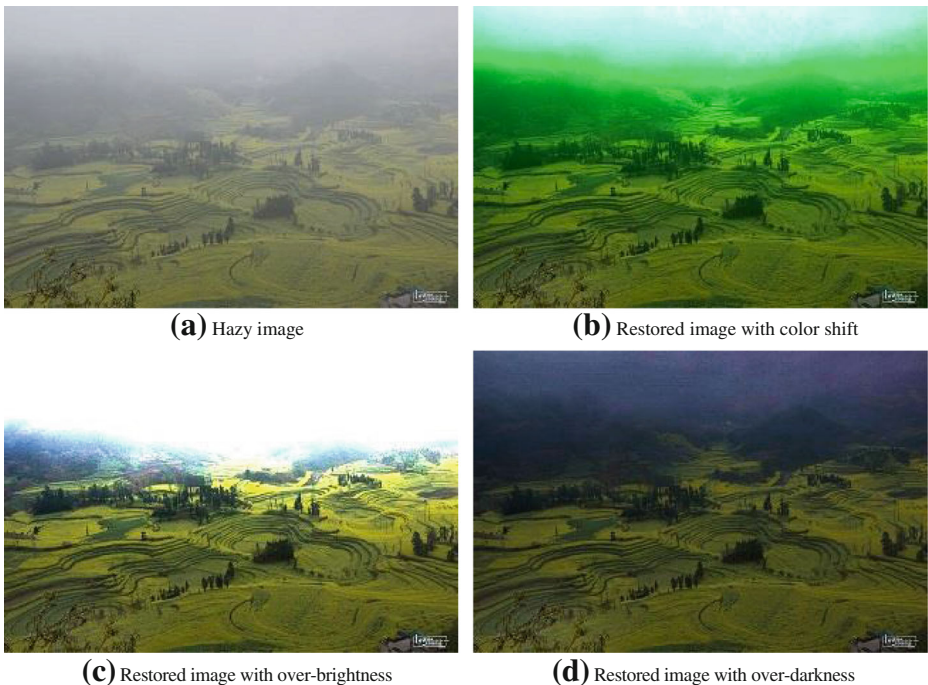

(**a**) Hazy image   (**b**) Restored image with color shift

(**c**) Restored image with over-brightness   (**d**) Restored image with over-darkness

Fig. 1 Effect of airlight value error on the restoration of an image

restoration, which is caused by the overly low airlight value; and (d) is the over-dark image after restoration, which is caused by the overly hight airlight value.

Therefore, accurate estimation of airlight in a hazy image has an important role in image dehazing. Based on the analysis of the gray characteristics of the sky region in the hazy image, an airlight search algorithm based on gray projection is presented to overcome the drawbacks of the current airlight acquisition method of low efficiency and large error. This algorithm applies a simple and effective filtering to obtain the total image gray distribution, utilizes the horizontal and vertical projections to locate the sky region, and obtains the airlight of the sky via a statistical method. The airlight value obtained by this algorithm is consistent with the airlight value selected by the human eye. The algorithm has significant application value due to its fast calculation speed and high robustness.

The rest of this paper is organized as follows: the dark channel prior theory and common methods for obtaining airlight are briefly introduced in Section 2. In Section 3, the airlight acquisition algorithm is proposed in this paper, which consists of three steps: fast average filtering, regional projection and airlight calculation. Section 4 provides the experimental results, and some conclusions are presented in the last section.

2 Related work

2.1 Dark Channel prior

In the application of computer vision, the physical model for describing hazy images usually be expressed as

$$I(x) = J(x)t(x) + A(1-t(x)) \tag{1}$$

where x is the coordinate of pixel, $I(x)$ is the hazy image, $J(x)$ is the clear image without fog, A is the airlight value, and $t(x)$ is the medium transmission.

The dark channel principle is an a priori statistical pattern based on a dehazed image [12], which contain the principle that most non-sky regions have at least one color channel with a very low intensity value approaching to zero. The formula can be expressed as

$$J^{dark}(x) = \min_{c \in \{r,g,b\}} \left(\min_{y \in \Omega(x)} (J^c(y)) \right) \rightarrow 0 \tag{2}$$

where J^c is the color channel of J, $\Omega(x)$ is the small image block centered on x, and J^{dark} is the dark channel image.

Assuming that great airlight A is known, the transmission $\widetilde{t}(x)$ in the small image block $\Omega(x)$ is constant. Then, Eq. (1) is divided by A^c. The conversion of $\min_{c \in \{r,g,b\}} \left(\min_{y \in \Omega(x)} () \right)$ according to Eq. (2) is expressed as follows:

$$\widetilde{t}(x) = 1 - \min_{c \in \{r,g,b\}} \left(\min_{y \in \Omega(x)} \left(\frac{I^c(y)}{A^c} \right) \right) \tag{3}$$

In actual practice, to retain a portion of residual fog to ensure that an image has the sense of depth of field, the correction factor $\omega(0 < \omega \leq)$ was imported, and Eq. (3) is re-expressed as follows:

$$\widetilde{t}\sim(x) = 1-\omega \min_{c\in\{r,g,b\}} \left(\min_{y\in\Omega(x)} \left(\frac{I^c(y)}{A^c} \right) \right) \tag{4}$$

Since the assumption of constant transmission in the local region causes the block effect in the calculated transmission map, guided filter [19] is usually used to obtain the optimized $t(x)$.

According to the airlight scattering model, once the transmittance $t(x)$ and the airlight A are obtained, the scene image can be restored according to Eq. (1).

$$J(x) = \frac{I(x)-A}{\max(t(x), t_0)} + A \tag{5}$$

To reduce the noise of the restored image, set $t_0 = 0.1$.

2.2 Current Airlight acquisition method

For the extraction of airlight values, researchers have proposed some effective methods. Narasimhan and Nayar [27] applied the human-computer interaction method to select a set of regions with the same color but different depths. This type of frequent operation enables this method to be applied to an actual scene. Fattal [8] proposed a user-assisted method that obtains the airlight intensity by selecting several image blocks of different albedo values and estimating the intersection of red-green-blue (RGB) planes that contain the pixels in the selected image block. He also presented a method that automatically estimates the airlight intensity. This method inherited the method described in the literature by automatically selecting image blocks with different albedo values and estimating the magnitude of airlight [35] by minimizing the correlation between the transmittance and the surface albedo. Wang and Fan [40] believed that the gray pixels in fog are present in the deepest region of the depth image and the smooth region of a hazy image and that the airlight is obtained by averaging the pixel values of the hazy gray region.

Tan [36] assumed that the brightest pixel in an image is saturated and estimated the airlight accordingly; however, the estimation failed when the image contains a white object. In the DCP method proposed in Ref. [12], the airlight is estimated from the pixels that correspond to the 0.1% dark primary color of the brightest region. Meng et al. [25] improved the method by selecting the maximum value of the three-channel RGB minimum value figure as the airlight value A. This type of inaccurate airlight estimation method directly causes incorrect medium transmittance. Tarel and Hautiere [37] conducted white balancing of an image and used the pure white light vector A = [18] for dehazing. Kim et al. [17] presented a quaternary tree decomposition method that selects the largest region of the gray mean value by continuously segmenting via the strategy of hierarchical search; however, the method fails for images of white objects in space [48]. Park et al. [30] improved the method via image transformation, which employs the minimum Euclidean norm to estimate a relatively reliable airlight value. Pedone and Heikkila analyzed statistics of airlight color frequency in a natural image [31]. The airlight color value was obtained according to a solution method for designing robustness. The calculation in this method is simple. Fattal [9], the color lines generated by the global regularity method is proposed. If the image reflects the albedo of a single surface or contains rich details, the color will change significantly [24]. Cheng et al. [4] proposed an airlight extraction method based on color analysis that selects candidate points by estimating the color probability in the YCbCr space; this method is simple and effective. Zhang et al. [49] proposed a potential light source method using clustering technique screening to obtain the airlight

through the mean value and set the geometric center as the light source. Zhang et al. [50] directly selected the maximum value of the dark channel in the double region of a hazy image as the airlight. Wang et al. [42] reselected the brightest pixel of image as the airlight by removing the white objects and sky region to reduce the impact on atmospheric light. In a previous study [22], the estimation problem of an atmospheric transmission image was transformed into a quadratic programming problem to obtain the optimal airlight intensity using the normalized steepest descent method with constraints.

Although these methods have attained a certain dehazing effect, the dehazing performance for a whole image decreased due to a large number of calculations or large errors.

3 Gray integral projection

3.1 Methodology

By observation, the total color of the hazy image is dim. The sky region shows characteristics of gray value, such as brightness and smoothness. To identify the smooth region with high brightness, the integral projection is applied to perform an analysis.

The integral projection function is the earliest and most commonly employed projection function; it replies the change of gray values in an image. Assuming that $I(x, y)$ represents the pixel value of the (x, y) coordinate point in the digital image, the horizontal integral projection function $S_h(y_0)$ along the horizontal projection line direction $y = y_0$ in the interval $[x_1, x_2]$ is expressed as

$$S_h(y_0) = \sum_{x=x_1}^{x_2} I(x, y_0) \tag{6}$$

Figure 2 shows the gray integral projection curve of the image in the horizontal and vertical directions.

In some cases, to describe the mean in the projection direction, it is often represented by the average projection function; the corresponding horizontal projection function $M_h(y_0)$ is expressed in Eq. (7).

$$M_h(y_0) = \frac{1}{x_2 - x_1} \sum_{x=x_1}^{x_2} I(x, y_0) \tag{7}$$

(a) Original image   **(b)** Gray projection   **(c)** Projected screening region
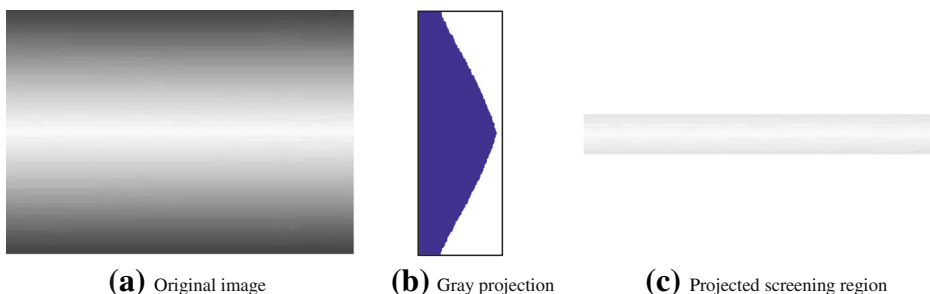
Fig. 2 Projected regional curve

To obtain a region with a large gray value, a method based on the maximum value of regional integration is proposed. If the hazy images are equally divided in the horizontal and vertical directions, the number of vertical segment is m, and the number of horizontal segment is n. After segmentation, the regional width of the horizontal direction is w, the vertical height is h, and the vertical projection function of region i and the horizontal projection function of region j are as follows:

$$(R_h)_j = \sum_{y=(j-1)h+1}^{iw} P_h(y) \qquad 1 \leq j \leq n \tag{8}$$

In Eq. (8), $P_h(y)$ represents the horizontal projection in the y-th row direction.

$$R(I, J) = \max\left[(R_h)_j\right] \tag{9}$$

where $i = 1, \ldots, m;\quad j = 1, \ldots, n$. As demonstrated by Eq. (9), the region obtained by projection is the maximum gray value. The projection process is shown in Fig. 3, where Fig. 3(a) displays the simulation of the gray distribution model for a hazy image; its gray distribution reduces from high to low. Figure 3(b) is the horizontal regional projection curve, where the region with the largest projection value is the candidate position, as shown in Fig. 3(c).

3.2 Analysis of anti-interference capability

Set X as a random variable; the size of its value corresponds to the pixel gray value in the image. Its mathemat ical expectations and variance are $E(X)$ and $\sigma^2(X)$, respectively. η is the independent random noise that satisfies the normal distribution $N(0, \sigma^2(\eta))$; then,

$$\begin{aligned}
\sigma^2(X + \eta) &= E(X + \eta - E(X))^2 \\
&= E(X - E(X))^2 + E(\eta^2) \\
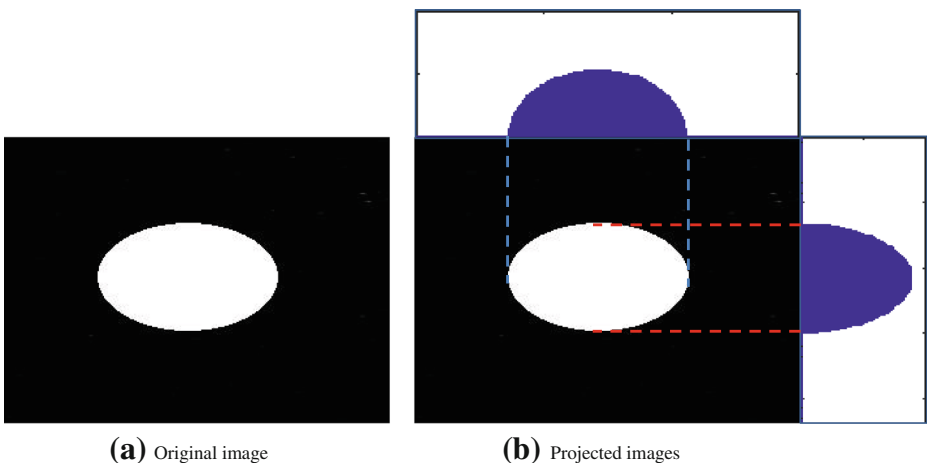&= \sigma^2(X) + \sigma^2(\eta)
\end{aligned} \tag{10}$$

(a) Original image   (b) Projected images

Fig. 3 Example of regional projection process

Therefore, the variance of the random variable for the k set in region R is

$$
\begin{aligned}
Var(R) &= \sum_{i=1}^{k} \sigma^2(X_i + \eta_i) \\
&= \sum_{i=1}^{k} \left(\sigma^2(X_i) + \sigma^2(\eta_i) \right) \\
&= \sum_{i=1}^{k} \sigma^2(X_i) + \sum_{i=1}^{k} \sigma^2(\eta_i)
\end{aligned}
\tag{11}
$$

The variance of the random noise $\sigma^2(\eta)$ is substantially smaller than $\sigma^2(X)$, that is, $\sigma^2(\eta) << \sigma^2(X)$; thus,

$$
\sum_{i=1}^{k} \sigma^2(X_i) + \sum_{i=1}^{k} \sigma^2(\eta_i) \approx \sum_{i=1}^{k} \sigma^2(X_i)
\tag{12}
$$

The gray projection method is not sensitive to random noise. To verify the anti-interference ability of this method, noise is added on hazy image. Figure 4 shows the results of sky region screening by projection method, in which, (a) displays a hazy image model. Figures 4(d), (g), and (j) represent Fig. 4(a) with the addition of various Gaussian noise (mean 0.1, variance 0.03), salt and pepper noise (intensity 0.05), and linear noise, respectively. The second column shows the subsequent horizontal gray projections of the four images and the third column contains four images with respect to the sky regional position results.

As shown in Fig. 4, the resulting projection curve will exhibit certain changes due to the impact of noise. Comparatively, the projection curves have many glitches and crests after noise was added. Due to the application of regional statistics, the results of the sky regional position before noise was added is consistent with the results of the sky regional position after noise was added. This finding indicates that the method has strong anti-interference ability and sturdy robustness compared with other methods.

4 Airlight estimation method

Based on the analysis, the flowchart of the fast airlight position method based on the gray projection is designed. To ensure position accuracy, the complexity of the algorithm can be reduced to enable its application to a real-time system [39]. The algorithm is divided into three modules: (1) gray transformation: the color image is transformed to a gray image; (2) sky region segmentation: based on the gray projection method, segmentation contains the sky region; and (3) calculation of the airlight value: the pixels in the sky region are counted to obtain the airlight intensity value. The entire dehazing algorithm flowchart is shown in Fig. 5.

The key steps are as follows:

Step 1: Since the image taken by the camera is a color image, gray processing during digitization is necessary to improve the computation speed, that is,

$$
Y = \omega_R * R + \omega_G * G + \omega_B * B
\tag{13}
$$

where $\omega_R = 0.299$, $\omega_G = 0.587$, and $\omega_B = 0.114$ are the corresponding weights of the color components R, G, and B, respectively.
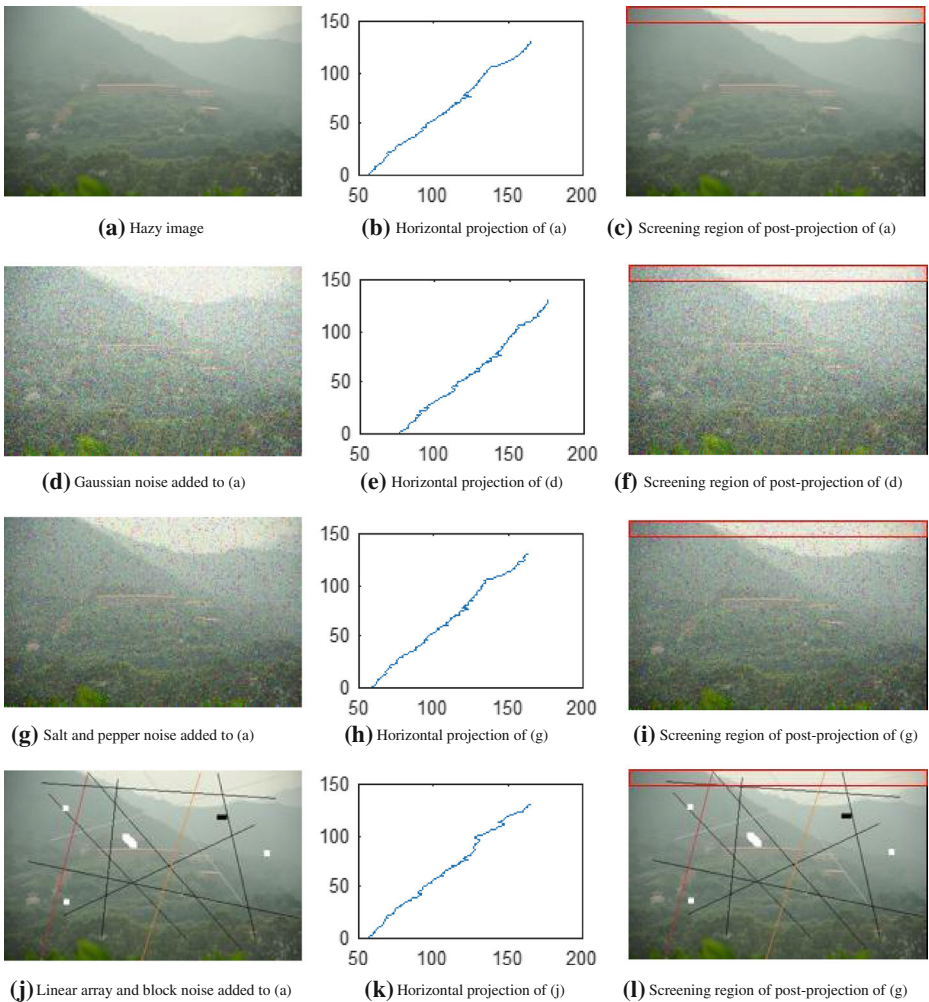
Fig. 4 Analysis of anti-interference capability for regional gray projection

Step 2: The resulting minimum filtered image is horizontally projected. Assume that image $I(x, y)$ is the input and the pixel size is $m \times n$; the horizontal projection is expressed as follows:

$$H(y) = \sum_{y=1}^{m} I(x, y) \ 1 \leq x \leq n \tag{14}$$

Step 3: The projection values are summed in the region of width $2b + 1$, and the region with themaximum value is screened, which can be expressed as follows:

$$H_{\max} = \max\left(\sum_{y=s-b}^{s+b} H(y)\right) b + 1 \leq s \leq m - b \tag{15}$$

Step 4: The cropped region is named as the image $K(x, y)$ with pixels number is $(2b + 1) \times n$. It's expression is:
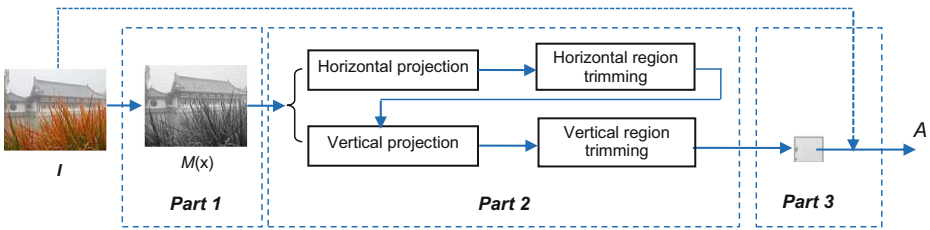
Fig. 5 Diagram of airlight calculation method

$$V(x) = \sum_{x=1}^{n} K(x, y) \; 1 \leq y \leq 2b + 1 \qquad (16)$$

Step 5: The vertical projection is implemented like Step 3, and the screened region is expressed as follows:

$$V_{\max} = \max\left(\sum_{x=s-b}^{s+b} V(x)\right) b + 1 \leq s \leq n - b \qquad (17)$$

The cropped region is named as image $R(x, y)$, and it's pixels number is $(2b + 1) \times (2b + 1)$.

Step 6: Compute the gray value of sky region. First, all the pixels in the sky region are collected, and those pixelvalues are sorted in descending order. Then, the mean gray value of the 10% pixels with the largest luminance in the sky region is treated as the airlight value A, and the expression is as follows:

$$A = mean\left(\max^{0.1} R(x)\right) \qquad (18)$$

This method can avoid the influence of a white cloud in the sky region to obtain a robust airlight value and eliminate the deviation caused by salt and pepper noise in the image. This process is shown in Fig.6.

Since the sum of all data in a certain region must be calculated after projection, repeated calculations will be performed between adjacent regions. To improve the computation speed, the acceleration algorithm of a box filter is applied. As shown in Fig. 7, assume that the data are listed as $i(x)(1 \leq x \leq n)$ with the width $(2b + 1)$ pixels; the sum of all gray values in this regions is expressed as follows:

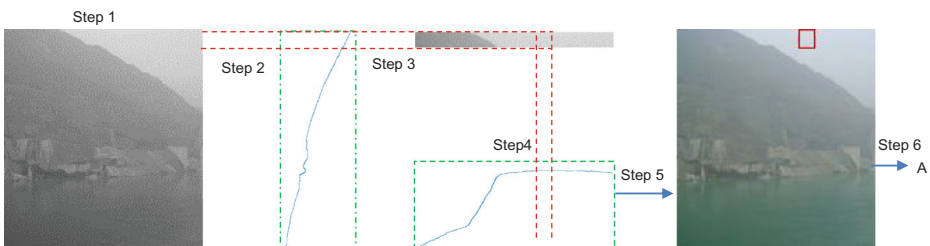$$Sum(t) = \sum_{x=t-b}^{t+b} i(x) \; b + 1 \leq t \leq n - b \qquad (19)$$

Fig. 6 Airlight calculation

Since a total of 2b repeated points $\{i(t-b+1), i(t-b+2), \ldots i(t+b-1)\}$ exist between adjacent regions $Sum(t-1)$ and $Sum(t)$, the previous region can be directly employed in the calculation and expressed as follows:

$$Sum(t) = Sum(t-1) - i(t-b) + i(t+b)b + 1 \leq t \leq n-b \tag{20}$$

Via box filtering, the summation operation is reduced from $(2b+1)$ to three times, which significantly accelerates the calculation speed.

5 Analysis of experimental results

To assess the performance of our method, we set up an experimental platform and wrote the codes with Matlab. The hardware of experimental platform is a Dell laptop with the processer Intel(R) i7-5500U CPU @ 2.4 GHz, and 8 Gbits RAM. The image dataset contains 1188 images, which were obtained from the Internet, involveing city streets, natural scenery, and aerial images. The images numbered from 0001.jpg to 1188.jpg, and some of them are shown in Fig. 8. The experiment results using the proposed airlight estimation method are shown in Fig. 9; the first and the third rows contain the hazy images, and the other rows contain the results. The corresponding sky areas are annotated by a red rectangle. Regardless of whether the image contains abrupt or smooth changes in the field of depth, the sky area obtained by this paper is consistent with observations made with the naked eye.

To objectively reflect the effectiveness of proposed method, the strategy of optimizing parameter is analyzed in this paper, and the comparisons between the proposed method and other methods are accomplished from the aspects of accuracy and computation complexity.

5.1 Accuracy comparison

Accuracy is an important indicator of the difference between the true airlight and estimated airlight with the proposed method. The value of airlight in the image is manually selected as the standard value, and the absolute value of the average difference between the estimated values and the manual values is used as the evaluation standard. The specific equation is expressed as follows:

$$Diff = \frac{1}{N} \sum_{i=1}^{N} |A_{man} - A_{com}| \tag{21}$$

where N is the number of experimental images, A_{man} is the manually selected airlight value, and A_{com} is the calculated airlight value. A smaller $Diff$ indicates that the value is closer to the true value.
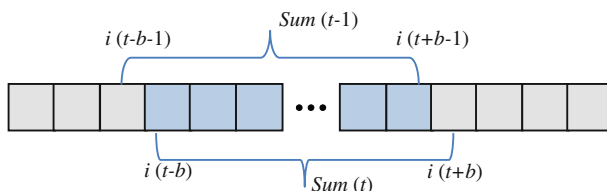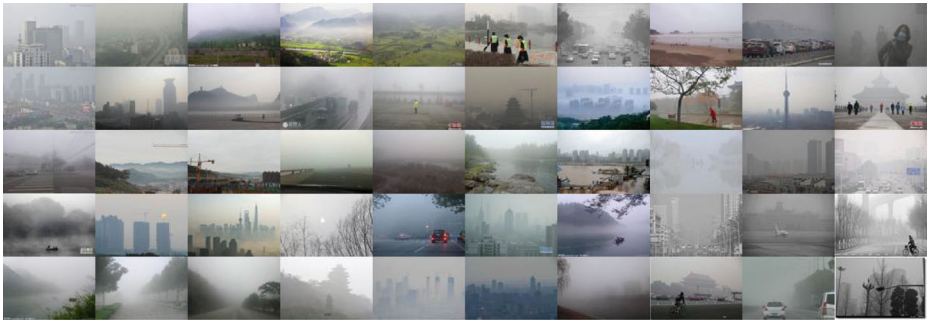

Fig. 7 Box filtering

Fig. 8 Experimental testing image set

5.1.1 Impact of parameter changes

According to the equation, the region width selection is important for gray integration because it directly affects the calculation accuracy. Different data were obtained by adjusting the region width in the experiment; the value of parameter b was set to 1/10 to 1/80 of the image size. Assuming that the total image vertical projection width is w, the change in b values is $\{(1/10) \times w, (1/15) \times w, \ldots, (1/75) \times w, (1/80) \times w\}$.

The selection of the airlight can use the maximum value method, average value method, or median value method, which can be expressed as follows.
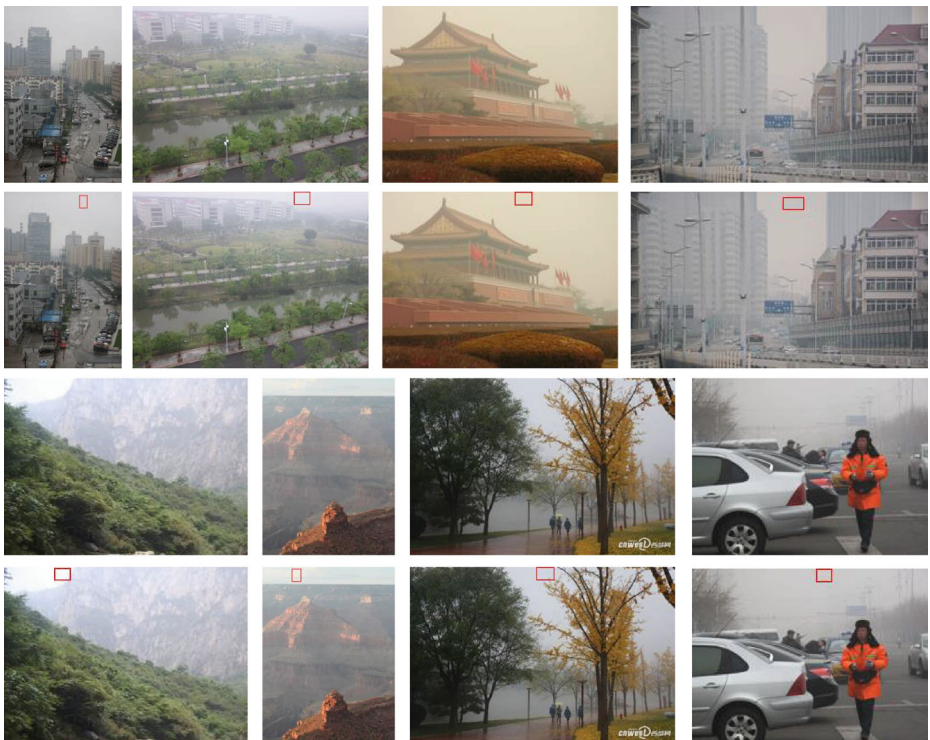

Fig. 9 Airlight value acquisition and dehazing results using the proposed method
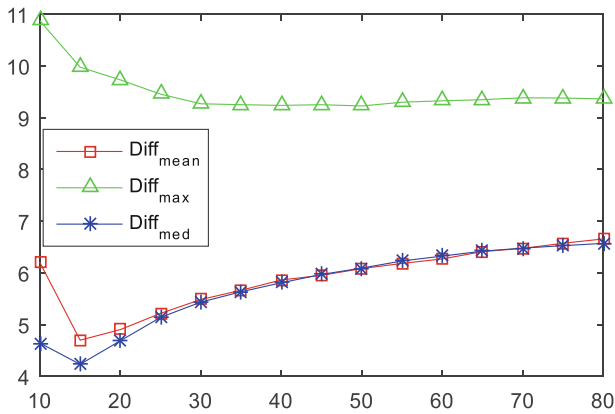
Fig. 10 Impact of parameter changes

The maximum value method:

$$A_{\max} = \max(R(x,y)) \tag{22}$$

The average value method:

$$A_{mean} = \mathrm{mean}(R(x,y)) \tag{23}$$

The median value method:

$$A_{med} = \mathrm{median}(R(x,y)) \tag{24}$$

All the 1188 images with different sizes were calculated using different methods; the curves of variations are shown in Fig. 10. The error in the data obtained by the maximum value method decreases as the number of blocks increase; however, the difference from the actual value is large. For the average and median value methods, the error increases as the number of blocks increase. The error starts to coincide when the number of blocks is 25 pixels; all minimum errors appeared at 15 pixels on the horizontal axis.

For the airlight value selection, the method of calculating the average value of a certain percentage of pixels within the region can also be employed. This paper employed two types of methods for the experiment. The first method sorts the pixel values in descending order, and

Table 1 Deviation Between The True Values and Calculated in Descending Order

b c	10	15	20	25	30	35	40	45	50	55	60	65	70	75	80
0.1	6.48	6.96	7.29	7.48	7.63	7.84	7.93	8.07	8.18	8.34	8.44	8.52	8.62	8.66	8.68
0.2	5.71	6.35	6.72	6.98	7.14	7.33	7.44	7.6	7.75	7.9	7.99	8.08	8.16	8.22	8.26
0.3	5.2	5.91	6.37	6.64	6.84	7.05	7.14	7.26	7.4	7.57	7.67	7.76	7.85	7.93	8.01
0.4	4.79	5.57	6.03	6.37	6.58	6.8	6.93	7.05	7.17	7.32	7.4	7.52	7.61	7.68	7.75
0.5	4.46	5.27	5.75	6.08	6.37	6.59	6.71	6.84	6.97	7.13	7.21	7.31	7.39	7.46	7.52
0.6	4.28	5.02	5.51	5.87	6.13	6.38	6.52	6.65	6.78	6.93	7.03	7.13	7.22	7.29	7.35
0.7	4.31	4.77	5.28	5.68	5.97	6.16	6.35	6.5	6.62	6.77	6.87	6.98	7.05	7.13	7.2
0.8	4.57	4.62	5.11	5.52	5.8	6	6.17	6.34	6.47	6.59	6.69	6.84	6.91	6.99	7.06
0.9	5.08	4.51	4.96	5.35	5.66	5.84	6.02	6.16	6.3	6.42	6.49	6.66	6.72	6.82	6.9
1	6.2	4.7	4.9	5.22	5.49	5.66	5.86	5.95	6.08	6.18	6.27	6.41	6.47	6.57	6.66

Table 2 Deviation between the True Values and Calculated in Ascending Order

b c	10	15	20	25	30	35	40	45	50	55	60	65	70	75	80
0.1	21.86	11.17	8.77	7.38	6.8	6.78	7.09	7.07	7.47	7.44	7.45	7.55	7.64	7.78	7.85
0.2	17.54	8.82	6.97	6.17	5.89	5.98	6.32	6.31	6.58	6.59	6.59	6.69	6.77	6.85	6.86
0.3	14.8	7.48	6.07	5.65	5.54	5.69	5.99	6.03	6.24	6.25	6.3	6.37	6.45	6.52	6.56
0.4	12.7	6.59	5.56	5.34	5.37	5.53	5.84	5.87	6.04	6.02	6.1	6.23	6.3	6.36	6.43
0.5	11.05	5.95	5.24	5.2	5.28	5.46	5.73	5.75	5.89	5.9	6.03	6.16	6.19	6.27	6.36
0.6	9.7	5.45	5.01	5.11	5.22	5.4	5.64	5.69	5.82	5.86	5.98	6.12	6.17	6.24	6.36
0.7	8.54	5.13	4.87	5.07	5.21	5.4	5.63	5.7	5.8	5.85	6	6.14	6.19	6.27	6.37
0.8	7.61	4.89	4.8	5.05	5.21	5.44	5.68	5.73	5.84	5.91	6.02	6.17	6.24	6.32	6.41
0.9	6.86	4.74	4.81	5.08	5.31	5.53	5.74	5.81	5.93	5.99	6.11	6.26	6.31	6.4	6.48
1	6.2	4.7	4.9	5.22	5.49	5.66	5.86	5.95	6.08	6.18	6.27	6.41	6.47	6.57	6.66

the second method sorts the pixel values in ascending order. The selected range of c is from 10% to100%, with the step of 10%. Thus, the former method selects points in the region with higher values, and the latter method selects points with a lower value. The size variation parameter ranges from 10 to 80 pixels, with a step size of five pixels. The data are shown in Tables 1 and 2. The average differences of different region widths are shown in Fig. 11. The error in the two sets of data gradually reduce as the value selection ratio increases. With the exception of the calculation obtained by selecting 10%, under the same ratio, the difference obtained by the ascending order selection method is smaller than the difference obtained by the descending order selection method.

5.1.2 Comparison with other methods

Based on the previous analysis, the parameter window parameter b is set to 15 pixels and the median value of the region is selected as the final airlight value. The proposed method is compared with some other methods, such as the Tan method [36], He method [12], Meng method [25], Kim method [17], Zhang method [50], and Wang method [42]. The average error after testing 1188 images is listed in Table 1. The errors of the Tan and Wang methods are significant. The errors for the He, Kim, and Zhang methods are similar. Our method obtained the smallest average error and highest accuracy compared to the true value.

5.2 Computational complexity

To verify the performance on running speed of proposed method, the computational complexity is also tested.
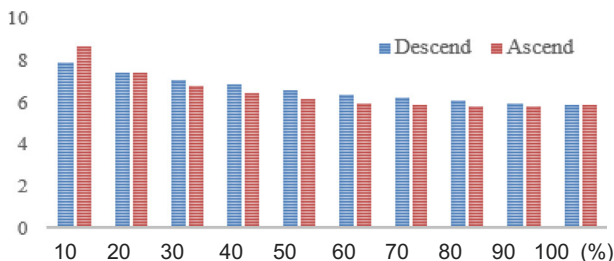

Fig. 11 Comparison of different value selection ranges

Table 3 Comparison of the Accuracy of Different Methods

Method	Tan [36] Method	He et al. [12] Method	Meng et al. [25] Method	Kim et al. [17]Method	Zhang et al. [50] Method	Wang et al. [42] Method	Proposed Method
Deviation	27.82	8.81	12.09	8.40	8.43	23.96	4.23

5.2.1 Comparison of total calculation results of all images

Different methods were used to perform calculations of 1188 images, and the Tan method [36], He method [12], Meng et al. [25] method, Kim et al. [17] method, Zhang et al. [50] method, and Wang et al. [42] method are used for comparison with the proposed method. To reflect the fairness of the operation, all programs were executed in a Matlab 2014 environment, and the accumulative calculation times of all images were cyclically recorded. As listed in Table 1, the lowest calculation efficiency and highest computation complexity were obtained for the He, Meng, and Zhang methods. This finding is primarily attributed to the existence of a two-dimensional minimum filtering operation, especially with the Meng method, which requires minimum filtering operations and achieves the highest computation complexity. The Tan method, Wang method, and proposed method have a high operation speed; the total operation time is approximately 20 s, which is approximately 1/75 of the operation time required by the Meng method. Therefore, the proposed method has an advantage with regard to absolute operation time. The operation times are listed in Tables 3 and 4.

5.2.2 Influence of image size on calculation results

To verify the running time of the algorithm as the image size increases, images of different sizes were employed for the experiment. Every image was repeated ten times, and the average value was selected. The calculation results are listed in Table 5, in which it can be seen that the proposed method have the highest computation speeds as Tan's method. When processing an image of 2048 × 1536 pixels, the proposed method only consumed 27 milliseconds. The time consumption of proposed method is only 1/73 of that of the Meng method when processing an image of 600 × 400 pixels. When processing a 2048 × 1536 pixels image, the proposed method consumed 1/276 of the time consumed by the Meng method. This finding indicates that the proposed method has high computation efficiency and can be applied in large-size image processing.

To compare the changing rate for time computation of different methods, the relative time change method is employed. Assuming that processing time of the smallest image is t_1, then the relative computation time is

**Table 4** Computational Complexity Comparison (Unit: s)

Method	Tan [36] Method	He et al. [12] Method	Meng et al. [25] Method	Kim et al. [17] Method	Zhang et al. [50] Method	Wang et al. [42] Method	Proposed Method
Time (s)	18.26	496.77	1504.03	32.98	643.65	21.06	19.43

Table 5 Comparison of Running Time on Different Methods(Unit:ms)

Methods Resolution	Tan [36] method	He et al. [12] method	Meng et al. [25] method	Kim et al. [17] method	Zhang et al. [50] method	Wang et al. [42] method	Proposed method
600 × 400	10.2	296.17	857.01	24.81	371.72	29.77	11.73
800 × 600	11.46	523.77	1487.44	32.63	600.16	30.91	12.4
1024 × 768	11.82	798.98	2296.12	40.21	920.84	31.89	13.57
1600 × 1200	15.56	1704.08	4994.61	76.91	1981.11	36.01	20.97
2048 × 1536	20.08	2700.65	7529.35	106.78	3096.27	40.33	27.24

$$T_r = t_n/t_1 \qquad (25)$$

where n is the image level, which increases as the image size increases.

Figure 12 shows the relative time curves of the Tan [36] method, He et al. [12] method, Meng et al. [25] method, Kim et al. [17] method, Zhang et al. [50] method, Wang et al. [42] method, and proposed method. It can be seen that, with the increasing of image size, the computation time of all methods increases gradually. The curves produced by the He, Meng, and Zhang methods have higher slopes than the curves produced by the remaining methods. The computation complexity nonlinearly increases as the image size increases. The variation trends of the Meng and He methods are similar due to the existence of a two-dimensional minimum value filtering operation. The slowest changes in computation complexity were observed for the Tan method, Wang method, and proposed method, especially for the Wang method, which only employed a linear operation on the data. Thus, its total trend is a straight line. The proposed method has a very high execution efficiency.

As demonstrated by the experimental results, the proposed method has the highest accuracy of airlight estimation. Although the proposed method is slightly inferior to the Tan method and the He method on the aspect of computational complexity, considering the large error in the accuracy of these two methods, the proposed method can take into account both the computation speed and the accuracy; thus, it is simple and feasible.
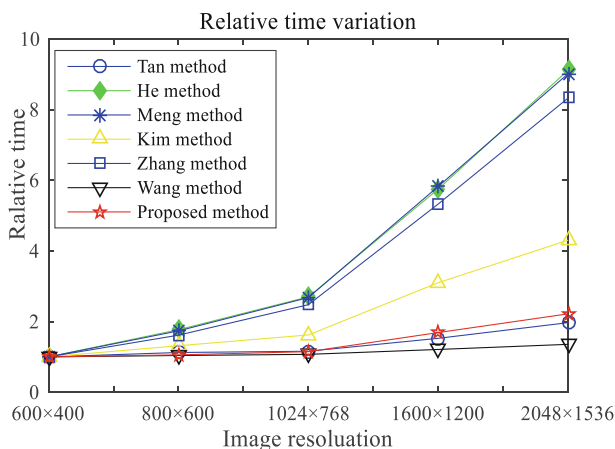
Fig. 12 Relative computation efficiency comparison

6 Conclusions

In the physical model-based image dehazing methods, the estimation of airlight value directly affects the image restoration quality. Based on the analysis of existing airlight estimation methods, this paper proposes a novel method that addresses the problems of low speed and large error. The proposed method used a gray projection framework on the sky area and utilizes statistics of the pixels within sky region to eventually obtain the airlight value. The experimental results proved the effectiveness and accuracy of this method. However, this method is limited to the condition that the hazy image has the sky regions. To improve the generalization ability and robustness, our future work is to experimentally analyze the influence of fog thickness and to study the methods of improving airlight estimation accuracy without sky regions.

Compliance with ethical standards

Competing interests The authors declare that they have no competing interests.

References

1. Alajarmeh A, Zaidan A (2018) A real-time framework for video Dehazing using bounded transmission and controlled Gaussian filter. Multimed Tools Appl 77(20):26315–26350. https://doi.org/10.1007/s11042-018-5861-4
2. Ancuti CO, Ancuti C (2013) Single image Dehazing by multi-scale fusion. IEEE Trans Image Process 22(8):3271–3282. https://doi.org/10.1109/TIP.2013.2262284
3. Cai B, Xu X, Jia K, Qing C, Tao D (2016) DehazeNet: an end-to-end system for single image haze removal. IEEE Trans Image Process 25(11):5187–5198. https://doi.org/10.1109/TIP.2016.2598681
4. Cheng F-C, Cheng C-C, Lin P-H, Huang S-C (2015) A hierarchical Airlight estimation method for image fog removal. Eng Appl Artif Intell 43:27–34. https://doi.org/10.1016/j.engappai.2015.03.011
5. Cooper TJ, Baqai FA (2004) Analysis and extensions of the Frankle-McCann Retinex algorithm. J Electron Imag 13(1):85–92. https://doi.org/10.1117/1.1636182
6. Dippel S, Stahl M, Wiemker R, Blaffert T (2002) Multiscale contrast enhancement for radiographies: Laplacian pyramid versus fast wavelet transform. IEEE Trans Med Imag 21(4):343–353. https://doi.org/10.1109/tmi.2002.1000258
7. X Dong, X Hu, S Peng, and D Wang (2010). Single color image dehazing using sparse priors," *IEEE Int. Conf. Image Process.*, Hong Kong, China, pp. 3593–3596, 2010
8. Fattal R (2008) Single Image Dehazing. ACM Trans Graph (TOG) 27(3):1–9. https://doi.org/10.1145/1360612.1360671
9. Fattal R (2014) Dehazing using color-lines. ACM Trans Graph 34(1):1–14. https://doi.org/10.1145/2651362
10. KB Gibson and TQ Nguyen (2013), "Fast single image fog removal using the adaptive wiener filter," *IEEE Int. Conf. Image Process.*, Melbourne, VIC, Australia, pp. 714–718, 2013
11. N Hautiere, J Tarel, and D Aubert (2007). "Towards fog-free in-vehicle vision systems through contrast restoration," *IEEE Conf. Comput. Vision Pattern Recognition*, Minneapolis, MN, USA, pp. 1–8, 2007

12. He K, Sun J, Tang X (2011) Single image haze removal using Dark Channel prior. IEEE Trans Pattern Anal Mach Intell 33(12):2341–2353. https://doi.org/10.1109/TPAMI.2010.168
13. He K, Sun J, Tang X (2013) Guided image filtering. IEEE Trans Pattern Anal Mach Intell 35:1397–1409. https://doi.org/10.1109/TPAMI.2012.213
14. Huang S, Chen B, Wang W (2014) Visibility restoration of single hazy images captured in real-world weather conditions. IEEE Trans Circuits Syst Video Technol 24(10):1814–1824. https://doi.org/10.1109/TCSVT.2014.2317854
15. Jessica E, Steven L, Jean-Baptiste T (2018) Color and sharpness assessment of single image Dehazing. Multimed. Tools Appl 77(12):15409–15430. https://doi.org/10.1007/s11042-017-5122-y
16. Jiang B, Meng H, Ma X, Wang L, Zhou Y, Xu P, Jiang S, Meng X (2018) Nighttime image Dehazing with modified models of color transfer and guided image filter. Multimed Tools Appl 77(3):3125–3141. https://doi.org/10.1007/s11042-017-4954-9
17. Kim J-H, Jang W-D, Sim J-Y, Kim C-S (2013) Optimized contrast enhancement for real-time image and video Dehazing. J Vis Commun Image Represent 24(3):410–425. https://doi.org/10.1016/j.jvcir.2013.02.004
18. Kim TK, Paik JK, Kang BS (1998) Contrast enhancement system using spatially adaptive histogram equalization with temporal filtering. IEEE Trans Consum Electron 44(1):82–87. https://doi.org/10.1109/30.663733
19. Kopf J, Neubert B, Chen B, Cohen M, Cohen-Or D, Deussen O, Uyttendaele M, Lischinski D (2008) Deep Photo: Model-Based Photograph Enhancement and Viewing. ACM Trans. Graph. (TOG) 27(5):116. https://doi.org/10.1145/1409060.1409069
20. L Kratz and K Nishino (2009). "Factorizing scene albedo and depth from a single foggy image," IEEE Twelth Int. Conf. Comput. Vision, Kyoto, Japan, pp. 1701–1708, 2009
21. Lee J, Li C, Lee H (2019) Visibility Dehazing based on channel-weighted analysis and illumination tuning. Multimed Tools Appl 78(2):1831–1856. https://doi.org/10.1007/s11042-018-6280-2
22. Li QH, Bi DY, Xu YL, Zha YF (2014) Haze Degraded Image Scene Rendition. Acta Autom Sinica 40:744–750. https://doi.org/10.3724/SP.J.1004.2014.00744
23. Li Z, Zheng J, Zhu Z, Yao W, Wu S (2015) Weighted guided image filtering. IEEE Trans Image Process 24(1):120–129. https://doi.org/10.1109/TIP.2014.2371234
24. Lu H, Li Y, Nakashima S, Serikawa S (2016) Single image Dehazing through improved tmospheric light estimation. Multimed Tools Appl 75(24):17081–17096. https://doi.org/10.1007/s11042-015-2977-7
25. G Meng, Y Wang, J Duan, S Xiang, and C Pan (2013), "Efficient image dehazing with boundary constraint and contextual regularization," IEEE Int. Conf. Comput. Vision, Sydney, NSW, Australia, pp. 617–624, 2013.
26. SG Narasimhan and SK Nayar (2003). "Interactive (de) weathering of an image using physical models," IEEE Int. Conf. Comput. Vision Workshop Color Photometric Methods Comput. Vision, New York, NY, pp. 1–7
27. Narasimhan SG, Nayar SK (2003) Contrast restoration of weather degraded images. IEEE Trans Pattern Anal Mach Intell 25(6):713–724. https://doi.org/10.1109/TPAMI.2003.1201821
28. SK Nayar and SG Narasimhan (1999). "Vision in Bad Weather," Proc. Seventh IEEE Int. Conf. Comput. Vision, Kerkyra, Greece, pp. 820–827
29. Nishino K, Kratz L, Lombardi S (2012) Bayesian Defogging. Int J Comput Vis 98(3):263–278. https://doi.org/10.1007/s11263-011-0508-1
30. H Park, D Park, DK Han, and H Ko (2014). "Single image haze removal using novel estimation of atmospheric light and transmission," IEEE Int. Conf. Image Process. (ICIP), Paris, France, pp. 4502–4506, 2014.
31. M Pedone and J Heikkilä (2011). "Robust airlight estimation for haze removal from a single image," IEEE Comput. Vision Pattern Recognition Workshops, Colorado Springs, CO, USA, pp. 90–96
32. YY Schechner, SG Narasimhan, and SK Nayar (2001). "Instant dehazing of images using polarization," IEEE Conf. Comput. Vision Pattern Recognition, Kauai, HI, USA, pp. 325–332
33. Seow M-J, Asari VK (2006) Ratio rule and Homomorphic filter for enhancement of digital colour image. Neurocomputing 69(7):954–958. https://doi.org/10.1016/j.neucom.2005.07.003
34. Shiau Y, Yang H, Chen P, Chuang Y (2013) Hardware implementation of a fast and efficient haze removal method. IEEE Trans Circuits Syst Video Technol 23(8):1369–1374. https://doi.org/10.1109/TCSVT.2013.2243650
35. M Sulami, I Glatzer, R Fattal, and M Werman (2014). "Automatic recovery of the atmospheric light in hazy images," IEEE Int. Conf. Comput. Photography (ICCP), Santa Clara, CA, USA, pp. 1–11, 2014.
36. RT Tan (2008). "Visibility in bad weather from a single image," IEEE Conf. Comput. Vision Pattern Recognit., Anchorage, AK, USA, pp. 1–8, 2008.

37. J Tarel and N Hautiere (2009). "Fast visibility restoration from a single color or gray level image," *IEEE Twelth Int. Conf. Comput. Vision*, Kyoto, Japan, pp. 2201–2208, 2009
38. Tripathi AK, Mukhopadhyay S (2012) Single image fog removal using anisotropic diffusion. IET Image Process 6(7):966–975. https://doi.org/10.1049/iet-ipr.2011.0472
39. W Wang, F Chang, T Ji, and X Wu, "A Fast Single-Image Dehazing Method Based on a Physical Model and Gray Projection," *IEEE Access*, vol.6, no.1, pp.5641–5653, doi. https://doi.org/10.1109/ACCESS.2018.2794340.
40. Wang Y, Fan C (2014) Single image defogging by multiscale depth fusion. IEEE Trans Image Process 23(11):4826–4837. https://doi.org/10.1109/TIP.2014.2358076
41. Wang Z, Feng Y (2014) Fast Single Haze Image Enhancement. Comput Electr Eng 40(3):785–795. https://doi.org/10.1016/j.compeleceng.2013.06.009
42. Wang J-B, He N, Zhang L-L, Lu K (2015) Single image Dehazing with a physical model and Dark Channel prior. Neurocomputing 149:718–728. https://doi.org/10.1016/j.neucom.2014.08.005
43. Wang W, Yuan X, Wu X, Liu Y (2017) Fast image Dehazing method based on linear transformation. IEEE Trans Multimedia 19(6):1142–1155. https://doi.org/10.1109/TMM.2017.2652069
44. Wang W, Yuan X, Wu X, Liu Y (2017) Dehazing for images with large sky region. Neurocomputing 238:365–376. https://doi.org/10.1016/j.neucom.2017.01.075
45. W Wang, X Yuan, X Wu, Y Liu, and S Ghanbarzadeh (2016). "An Efficient Method for Image Dehazing," *IEEE Int. Conf. Image Process. (ICIP)*, Phoenix, AZ, USA, pp. 2241–2245, 2016.
46. Yeh C-H, Kang L-W, Lee M-S, Lin C-Y (2013) Haze effect removal from image via haze density estimation in optical model. Opt Express 21:27127–27141. https://doi.org/10.1364/OE.21.027127
47. J Yu, C Xiao, and D Li (2010). "Physics-based fast single image fog removal," *IEEE Tenth Int. Conf. Signal Process. Proc.*, Beijing, China, pp. 1048–1052
48. Yuan H, Liu C, Guo Z, Sun Z (2017) A region-wised medium transmission based image Dehazing method. IEEE Access 5:1735–1742. https://doi.org/10.1109/ACCESS.2017.2660302
49. Zhang W, Hou X (2018) Light source point cluster selection-based atmospheric light estimation. Multimed Tools Appl 77(3):2947–2958. https://doi.org/10.1007/s11042-017-4547-7
50. Zhang XG, Tang ML, Chen H, Tang HZ (2014) A Dehazing method in single image based on double-area filter and image fusion. Acta Automat Sin 40:1733–1739. https://doi.org/10.3724/SP.J.1004.2014.01733
51. Zhu Q, Mai J, Shao L (2015) A fast single image haze removal algorithm using color attenuation prior. IEEE Trans Image Process 24(11):3522–3533. https://doi.org/10.1109/TIP.2015.2446191